Chemical Engineering Journal 477 (2023) 147208

Contents lists available at ScienceDirect

Chemical Engineering Journal

journal homepage: www.elsevier.com/locate/cej

Side chain modulated carbazole-based bifunctional hole-shuttle interlayer simultaneously improves interfacial energy level alignment and defect passivation in high-efficiency perovskite solar cells

Yuan-Yu Chiu [a], Shih-Hsuan Chen [a], Kun-Mu Lee [a,b,c], Tz-Feng Lin [d], Ming-Chung Wu [a,b,c,e,*]

[a] Department of Chemical and Materials Engineering, Chang Gung University, Taoyuan 33302, Taiwan
[b] Center for Sustainability and Energy Technologies, Chang Gung University, Taoyuan 33302, Taiwan
[c] Division of Neonatology, Department of Pediatrics, Chang Gung Memorial Hospital at Linkou, Taoyuan 33305, Taiwan
[d] Department of Fiber and Composite Materials, Feng Chia University, Taichung 40724, Taiwan
[e] Department of Materials Engineering, Ming Chi University of Technology, New Taipei City 24301, Taiwan

ARTICLE INFO

Keywords:
Perovskite solar cell
Carbazole
Defect states
Passivation
Side chain-modulated

ABSTRACT

Perovskite solar cells have reached a power conversion efficiency over 26.1 %, and the interface engineering between perovskite and hole transport layer (HTL) is crucial for achieving high performance. There exists a noticeable research gap when it comes to designing an interlayer layer that can both hold defect passivation and hole transportability. To bridge this gap, we have designed and synthesized two functional molecules with carbazole cores and side chain modifications, namely CVE-Br and CVE-DPA. Beyond the suitable energy levels of the carbazole group, CVE-Br can intercalate into perovskite lattice, create a low-dimensional perovskite, and further minimize defects. Instead of forming low dimensional structure, CVE-DPA molecule wraps around the perovskite. That makes it passivate perovskite defects and facilitate hole transport without the limitation of carrier transportation. As a result, the power conversion efficiency of perovskite solar cells with CVE-DPA can achieve 22.05 %. The hydrophobicity of CVE-DPA confers the corresponding devices to retain 87 % of the initial efficiency after 1000 h.

1. Introduction

Over the past decade, perovskite solar cells (PSCs) have attracted enormous attention due to their exceptional optoelectronic properties, including superior photon harvesting capabilities, remarkably long charge carrier diffusion lengths, and a tunable bandgap [1–3]. The power conversion efficiency (*PCE*) of PSCs has been busted from 3.8 % to an impressive 26.1 % within a few years [4–6]. However, the presence of a high density of defects in the perovskite thin film crystals imposes limitations on enhancing the *PCE* of PSCs beyond the theoretical limit set by the Shockley-Queisser theory, which stands at approximately 33 %. Reducing the defect density in the perovskite material and improving the long-term stability of perovskite solar cells emerge as a viable method to approach the theoretical limit of single-junction solar cells [7,8].

Defects both internally and on the surface [9] fall into two main categories: (i) Deep-level traps, including under-coordinated Pb^{2+}, I^-, grain boundaries (GBs), and metallic lead (Pb^0). During device fabrication and operation, the escape of organic cations and halides can lead to PbI_2 at the surface and GBs of the perovskite or the formation of under-coordinated Pb^{2+} ions. Excessive PbI_2 on the perovskite surface can induce perovskite decomposition [10–12], while under-coordinated Pb^{2+} can act as non-radiative recombination centers [13]. Additionally, Pb^{2+} is prone to undergo reduction reactions, forming deep defect states of metallic Pb^0 [14,15]. These deep energy level traps can capture electrons and holes, triggering non-radiative recombination processes and resulting in a sharp decrease in efficiency. (ii) Shallow-level traps mainly consist of point defects such as I^- vacancies and MA^+ vacancies. Although these shallow-level defects have a negligible effect on non-radiative recombination, their migration within GBs has been observed under external electric fields, intense illumination, and elevated temperatures. This migration has adverse implications for *PCE* and stability [9]. Therefore, employing suitable materials for interface defect passivation is important to mitigate non-radiative recombination

* Corresponding author at: Department of Chemical and Materials Engineering, Chang Gung University, Taoyuan 33302, Taiwan.
E-mail address: mingchungwu@cgu.edu.tw (M.-C. Wu).

https://doi.org/10.1016/j.cej.2023.147208
Received 8 August 2023; Received in revised form 2 November 2023; Accepted 6 November 2023
Available online 7 November 2023

and fabricate high-efficiency perovskite solar cells.

Effective defect passivation in perovskite materials can be achieved through both coordination bonding or ionic bonding [9,16]. The presence of under-coordinated Pb^{2+} in the perovskite structure allows it to accept electrons as a Lewis acid. Lewis bases are capable of donating a pair of nonbonding electrons to coordinate and passivate under-coordinated Pb^{2+} or Pb clusters. [17]. Introducing Lewis bases such as 2-(methylthio)ethylamine hydrochloride (MTEACl) and sulfur atoms in thiophene molecules to donate nonbonding electrons and coordinate with under-coordinated Pb^{2+} or Pb clusters, thereby passivating defects and exhibiting strong electronic interactions with Pb^{2+}, enhancing the overall *PCE* to 17.17 % and 18.01 % [18,19]. Pyridine-based molecules are other commonly Lewis bases which passivate defects by leveraging the unoccupied electron on the nitrogen (N) atom, resulting in the increase of the device's *PCE* to 20.79 % and 22.10 % [20–22]. Further, molecules containing OCH_3 and C = O functional groups coordinate with under-coordinated Pb^{2+} through the lone pair electrons on the oxygen(O) atom. This coordination effectively passivates defects in perovskite, leading to an increased efficiency of up to 24.30 % and enhanced stability [23–30]. In addition to surface defects, the penetration of water molecules significantly impacts the photovoltaic conversion efficiency and long-term stability of perovskite solar cells [31]. Meanwhile, water infiltration triggers a phase transition of $FAPbI_3$ from the desirable α-phase to the less favorable δ-phase [32], hindering charge transport in $FAPbI_3$ perovskite crystals. Thus, molecules possessing hydrophobic properties and defect passivation capabilities are crucial for enhancing the stability of $FAPbI_3$ crystals.

Furthermore, amphiphilic molecules with long alkyl chains and ammonium functional groups, such as 3-aminopropyltrime-thoxysilane, have the advantage of simultaneously passivating Pb^{2+} and increasing hydrophobicity [33]. Similarly, phenethylammonium iodide (PEAI) [34] and 2-bromophenethylammonium iodide (2-Br-PEAI) [35] have been extensively used as passivating agents for halogen vacancies in perovskite materials through long alkyl chains and ammonium functional groups. This interface engineering results in enhanced efficiency of 23.32 % and 24.22 %, respectively, along with improved long-term stability. However, the use of long alkyl chains as passivation materials may lead to a decrease in photovoltaic performance due to their higher exciton binding energy (i.e., larger energy bandgap), and deteriorate charge transport capabilities [36,37]. To address this, dual-functional passivating materials capable of simultaneously passivating defects, enhancing hydrophobicity, and facilitating charge transfer have attracted significant attention. For instance, a 2,8-dibromoindeno-(1,2-b)fluorene-6, 12-dione core grafted with dimethoxytriphenylamine (TPA) effectively passivates Pb^{2+} and improves charge transport properties resulting in an efficiency increase to 19.74 % [27]. Another example is N-((4-(N,N,N-triphenyl)phenyl)ethyl)ammonium bromide (TPA-PEABr), synthesized by grafting TPA moieties with ammonium functional groups and bromine atoms, which can passivate I^- and MA^+ defects, leading to an efficiency increase to 18.15 % [38]. 2DP-PDI has pyromellitic diimide at its core with multiple carbonyl functional groups attached which improves efficiency up to 24.20 % by utilizing carbonyl passivation on defects as well as intermolecular π-π stacking interactions [39]. When it comes to materials that enhance charge transport, the carbazole group is commonly employed due to its low cost, excellent charge transport capability, chemical stability, and ease of modification with various functional groups [20,40–42]. Specifically, within the structures of dimethoxydiphenylamine and dimethoxytriphenylamine, the presence of methoxy groups not only assists in passivating perovskite defects but also facilitates efficient intra-molecular charge transfer, thereby increasing the charge transport efficiency of the material. These functional groups have become widely used as side-chain functional groups in the design of modifying layers and hole-transporting materials (HTMs) [29,43–45].

The exceptional photovoltaic properties of carbazole derivatives have clearly captured significant attention in the realm of optoelectronic applications. However, while most research in this area tends to focus on either defect passivation in perovskites or the enhancement of hole transport efficiency, there remains a notable gap. Few have ventured into designing carbazole-based derivatives that excel both as passivation materials and in exhibiting hole transport properties. In our study, we have synthesized 2,7-dibromocarbazole, illustrating its potential for dual functionality.

In this study, we developed a series of compounds with a central carbazole group and hydrophobic long alkyl chains, grafted with 2-chloroethyl vinyl ether (CVE). First, we synthesized 2,7-dibromo-9-(2-(vinyloxy)ethyl)-9H-carbazole (CVE-Br) by grafting the hydrophobic 2-chloroethyl vinyl ether onto the carbazole core. Subsequently, we replaced the bromine atoms on CVE-Br with 4,4′-dimethoxy-diphenylamine groups to synthesize N2,N2,N7,N7-tetrakis(4-methoxyphenyl)-9-(2-(vinyloxy)ethyl)-9H-carbazole-2,7-diamine (CVE-DPA). We investigated the molecular stacking, structure, and interactions between these two materials and the perovskite by grafting various functional groups onto the carbazole moiety. Both CVE-Br and CVE-DPA possess suitable energy levels, while the carbazole group in these compounds provides effective hole transport. The long alkyl chains on the carbazole unit also enhance the hydrophobicity of the devices. In CVE-DPA, the presence of 4,4′-dimethoxy-diphenylamine effectively passivates perovskite defects and enhances hole transport efficiency. As a result, the devices exhibited excellent performance with an efficiency of 22.05 % and retained over 87 % of their initial efficiency even after 1,000 h, demonstrating superior stability.

2. Results and discussion

The synthesis of CVE-Br was carried out as follows: 2,7-dibromocarbazole (1.39 g, 4.2 mmol) and K_2CO_3 (1.10 g, 8.0 mmol) were added to a reaction flask containing 25 mL of DMF. The temperature of the reaction flask was raised to 110 °C, and the color of the solution gradually changed from transparent to pale yellow, indicating the protonation and substitution of the starting material in the presence of an organic base. The mixture was stirred and heated for an additional 30 min. Then, CVE (0.64 g, 6.06 mmol) was added to the reaction flask, and the reaction was allowed to proceed at a constant temperature for 16 h. After natural cooling, the product appeared as a deep yellow solid. The target product was separated by column chromatography, resulting in a white powder with a yield of 70 %, as shown in Fig. 1(a).

The synthesis of CVE-DPA was performed using the Buchwald-Hartwig cross coupling reaction. In a clean reaction flask, CVE-Br (1.73 g, 4.4 mmol), 4,4′-dimethoxy-diphenylamine (2.08 g, 9.0 mmol), sodium t-butoxide (0.87 g, 9.0 mmol), and the catalyst bis(tri-*tert*-butylphosphine) palladium (0) (10 mg, 20 μmol) were added. Then, 25 mL of toluene was added to the flask. The temperature of the reaction flask was raised to 110 °C, and the reaction mixture was heated for one day. The color of the solution in the reaction flask changed from yellow to dark brown. The target product was separated by column chromatography, resulting in a black powder with a yield of 40 %. The synthesis scheme was shown in Fig. 1(a).

To confirm the successful synthesis of the carbazole derivatives, the ^1H nuclear magnetic resonance (^1H NMR) spectrum is shown in Fig. 1(b, c). CVE-Br: ^1H NMR (600 MHz, $CDCl_3$, δ): 7.78–7.77 (d, 2H; CH), 7.58 (d, 2H; CH), 7.35 (d, 2H; CH), 6.39–6.35 (m, 1H; OCH), 4.40–4.50 (t, 2H; NCH_2), 4.15–4.10 (d, 1H; CH), 4.05–4.00 (t, 2H; OCH_2), 4.00–3.95 (d, 1H; CH) ppm. CVE-DPA: ^1H NMR (600 MHz, DMSO-d6, δ): 7.77–7.74 (d, 2H; CH), 7.01–6.95 (m, 10*H*; CH), 6.89–6.84 (m, 8H; CH), 6.67–6.65 (d, 2H; CH), 4.84–4.81 (m, 1H; OCH), 3.95 (m, 2H; CH_2), 3.75–3.68 (s, 12H; OCH_3), 3.63 (t, 2H; OCH_2), 3.50 (m, 2H; CH) ppm.

The ^{13}C nuclear magnetic resonance (^{13}C NMR) spectrum is shown in Fig. 1(d, e). CVE-Br: ^{13}C NMR (600 MHz, $CDCl_3$, δ): δ 151.11, 141.67, 122.97, 121.47, 119.87, 113.82, 112.28, 87.37, 65.67, 61.23. CVE-DPA: ^{13}C NMR (600 MHz, DMSO-d6, δ): 154.95, 145.87, 141.72, 141.21, 130.25, 125.37, 119.82, 117.11, 114.71, 114.58, 102.18, 80.68, 58.90,

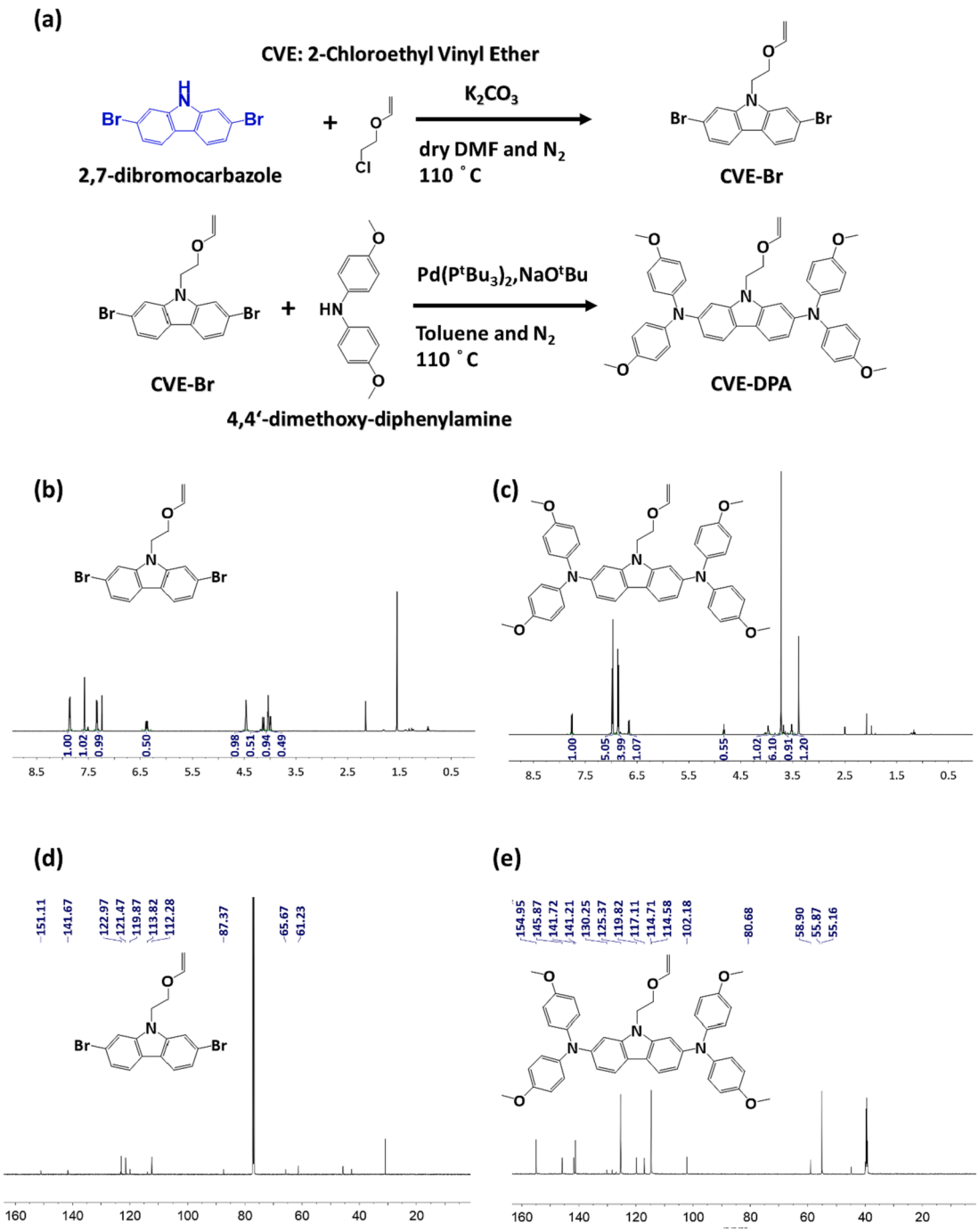

Fig. 1. (a) Chemical structures and the synthetic routes of CVE-Br and CVE-DPA. (b) ^{1}H NMR of CVE-Br, (c) ^{1}H NMR of CVE-DPA, (d) ^{13}C NMR of CVE-Br, and (e) ^{13}C NMR of CVE-DPA.

55.87, 55.16.

To investigate the influence of attaching carbazole derivatives on the morphology and photovoltaic properties of perovskite films, surface morphology was analyzed using scanning electron microscopy (SEM), energy-dispersive X-ray spectroscopy (EDS) mapping and atomic force microscopy (AFM). Images are shown in Fig. 2 and Figs. S1-S4. SEM images reveal that the surface of the perovskite film coated with CVE-Br has an needle-like structure compared with control, while the surface of the CVE-DPA perovskite film exhibits a uniform film morphology. The cross-sectional SEM image of the corresponding perovskite film is shown in Fig. S5. In order to explore why there is such an obvious difference between the perovskite film spin-coated with carbazole derivatives and control, we used EDS mapping to observe the elemental distribution of the film surface. Based on EDS mapping observations in Figs. S1-S3, it was found that the distribution of elements on the surfaces of CVE-Br and CVE-DPA perovskite films is similar to that of the control sample. It is noteworthy that the ratio of oxygen atoms on the surface of CVE-DPA increased from 0.11 %, control, to 0.77 %. This indicates that CVE-DPA still exhibits a high concentration distributed on the perovskite surface. To further understand the bright spots on the SEM images of the control and CVE-Br surfaces, we conducted elemental analysis at the positions indicated in Fig. S4. From Fig. S4(a) and Table S1, it can be observed that the average ratio of Pb at the bright spots (labeled 1–5) in the SEM is 33.26 %, which is slightly lower than the average ratio of Pb

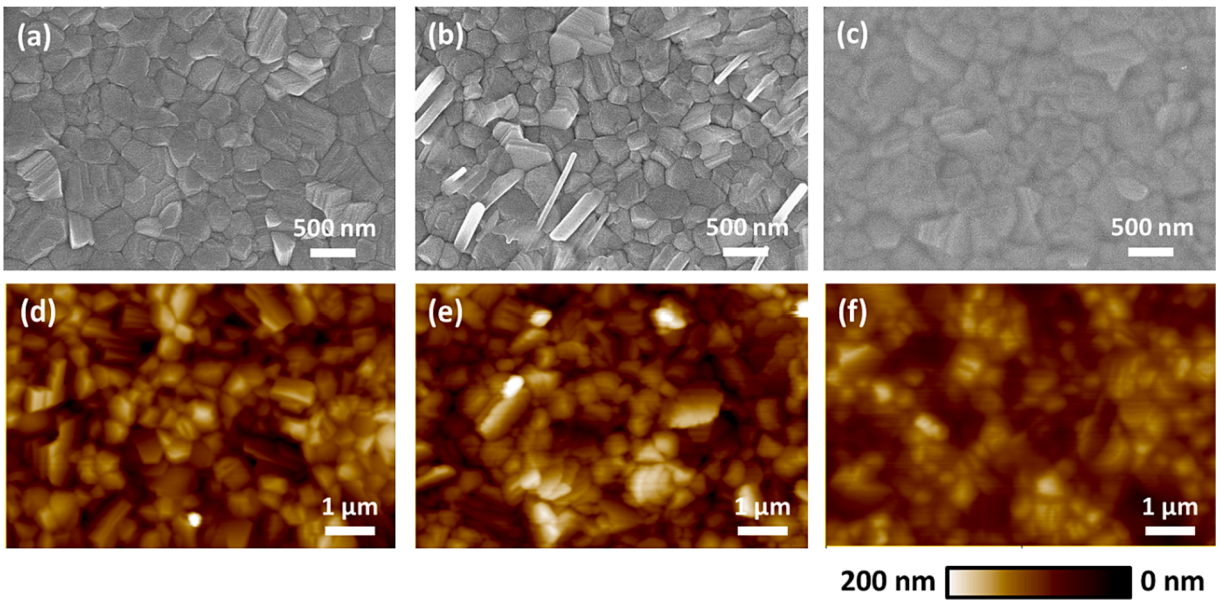

Fig. 2. Top view SEM images of perovskite thin films (a) without carbazole derivative (control), (b) with CVE-Br, and (c) with CVE-DPA. AFM analysis of FTO substrate supported perovskite films (d) control, (e) with CVE-Br, and (f) with CVE-DPA.

at the normal surface regions (labeled 6–8), which is 34.35 %. This suggests that the bright spots are not PbI_2 but exhibit a perovskite structure. It has been reported that the needle-like bright spots on the surface can be attributed to the formation of low-dimensional perovskite structure [46–48]. Analyzing Fig. S4(b) and Table S2, it can be observed that in CVE-Br, the average ratio of Br at the needle-like bright spots is 1.80 %, which is higher than the average ratio of Br on the flat surface, which is 1.41 %. Based on these results, we conclude that the needle-like bright spots in CVE-Br are attributed to the interaction between Br atoms and the perovskite, forming a low-dimensional perovskite structure within CVE-Br [35,49]. Also, AFM analysis indicates that perovskite film coated with CVE-Br exhibits a root mean square (RMS) roughness of 30.14 nm, approximately 6 % higher than that of the control sample at 28.25 nm. It is attributed that the needle-shaped low-dimensional perovskite results in the uneven surface of the perovikite film, thereby increasing the surface roughness of CVE-Br. In comparison, after the CVE-DPA treatment, some of the CVE-DPA penetrates the defects on the perovskite surface, leading to a flatter morphology as the pore defects get filled, with a root-mean-square roughness of 23.05 nm, significantly lower than the control sample. Results indicate that the application of CVE-DPA on the surface of the perovskite active layer effectively reduces roughness, which is crucial for preventing current leakage and enhancing the charge collection efficiency of the photovoltaic device [29,41]. To clarify the interactions between carbazole derivatives and the perovskite crystals, subsequent analysis utilized X-ray diffraction (XRD), grazing-incidence wide-angle X-ray scattering (GIWAXS), and X-ray photoelectron spectroscopy (XPS).

XRD analysis is shown in Fig. 3(a). The XRD diffraction peaks exhibit significant characteristic peaks of the perovskite film following treatment with carbazole derivatives. The crystallite size of each plane in Fig. 3(a) is estimated using Debye–Scherrer equation. The Debye-Scherrer equation is as follows:

$$D_{hkl} = \frac{K\lambda}{\beta_{hkl} cos\theta} \quad (1)$$

where D is the crystalline size, K represents the dimensionless shape factor, λ denotes the X-ray wavelength, β denotes the full width at half maximum (FWHM), and θ is the Bragg's angle.

The crystal size of perovskite film with CVE-Br for 101.3 nm and perovskite film with CVE-DPA for 107.8 nm, in contrast to the original perovskite crystal for 106.3 nm.

To understand the microstructure and crystal growth orientation of perovskite film with CVE-Br and CVE-DPA, grazing-incidence wide-angle X-ray scattering (GIWAXS) was performed for advanced analysis. GIWAXS provides an increased path length of X-rays within the thin film, making it more suitable for analyzing thin film materials compared to conventional theta-2theta mode [50]. Fig. 3(b,c,d) displays the 2D diffraction patterns of the control sample, perovskite film with CVE-Br, and CVE-DPA, respectively. The perovskite films treated with various carbazole derivatives exhibited well-defined Bragg peaks at q_z ~10.0 and 20.0 nm^{-1}, corresponding to highly oriented perovskite grains aligned with the (100) and (200) diffraction peaks, while q_z ~14.2, 17.4, and 22.2 nm^{-1} corresponded to the (110), (111), and (210) diffraction peaks, respectively, indicating the isotropic orientation of perovskite microcrystals [6,51]. In the case of the perovskite film with CVE-Br, low-dimensional perovskite diffraction peaks appeared at q_z ~4.8, 6.3, and 12.8 nm^{-1}, as shown in Fig. 3(c, e) (zoomed image in Fig. S6). This suggests that the Br atoms in CVE-Br can interact with the perovskite, forming a low-dimensional perovskite structure. However, these diffraction rings are attributed to Debye-Scherrer diffraction, indicating that the low-dimensional perovskite crystals within the CVE-Br perovskite film are randomly oriented [51]. This finding aligns with the observation of low-dimensional perovskite crystals on the surface of the CVE-Br perovskite film using SEM and AFM. As suggested, perovskite film with CVE-DPA does not penetrate the perovskite, instead, it merely covers the surface of the perovskite film.

To investigate the energy levels of CVE-Br and CVE-DPA, UV–Vis spectra, ultraviolet photoelectron spectroscopy (UPS), and Tauc-plots measurements were conducted and illustrated in Fig. S7. Carbazole derivatives are important moieties in improving the device performance by facilitating band alignment between the perovskite layer and HTL. This band alignment not only reduces interface carrier losses but also enhances carrier extraction and separation [52,53]. The energy level diagram clearly shows that CVE-Br and CVE-DPA exhibit suitable highest occupied molecular orbital (HOMO) energy levels of −5.19 eV and −5.17 eV, respectively. These energy levels facilitate efficient hole transfer from the perovskite layer to the HTL. It should be noted that the energy levels of the perovskite layer may vary due to defect passivation. UV–Vis absorption and Tauc-plots measurements of the perovskite layer with control, CVE-Br, and CVE-DPA were measured for comparison,

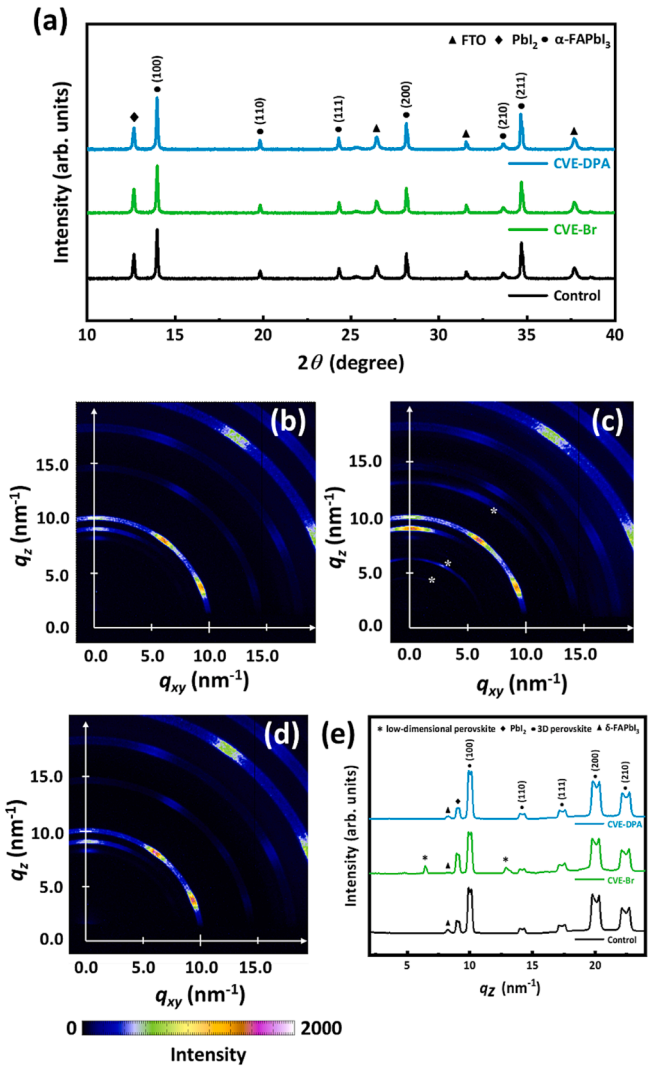

Fig. 3. (a) XRD patterns of control and carbazole derivatives perovskite layers. 2D GIWAXS patterns of perovskite layers (b) control and (c) with CVE-Br, (d) with CVE-DPA. (e) 1D GIWAXS spectra (Q vector) for the control, perovskite layers with CVE-Br, and CVE-DPA. The * represents the low-dimensional perovskite peak position.

shown in Fig. S8. UPS was used to measure the valence band maximum (VBM) of perovskite films coated with control, CVE-Br, and CVE-DPA, shown in Fig. 4(a-f). The corresponding energy level diagram is presented in Fig. 4(g). The VBM of the untreated perovskite film is approximately −5.59 eV, while the VBM of the perovskite films coated with CVE-Br and CVE-DPA is −5.55 eV and −5.52 eV, respectively, indicating appropriate band bending. It is speculated that the dipole moments of CVE-Br and CVE-DPA influence the VBM of the perovskite layer [54], further demonstrating their ability to adjust the energy levels within the device and enhance charge transfer efficiency. The absorption peaks of CVE-Br and CVE-DPA were observed between 320 and 360 nm for π-π* transitions, while the absorption peak near 380 nm for CVE-DPA arose from intramolecular charge transfer from the 4,4‘-dimethoxy-diphenylamine moiety to the carbazole moiety (Fig. S7(g)). The strong electronic transfer promotes hole withdrawing.

Next, XPS analysis was performed to confirm the interaction between the carbazole derivatives and surface defects in the perovskite films. From the Pb *4f* spectrum, two main peaks were observed at the binding energies of 142.9 eV and 138.1 eV corresponding to Pb $4f_{5/2}$ and Pb $4f_{7/2}$, as shown in Fig. 5(a). Upon the addition of CVE-Br, the binding energies of Pb $4f_{5/2}$ and Pb $4f_{7/2}$ shift towards lower binding energies of 142.5 eV and 137.6 eV. The shifting of Pb $4f_{5/2}$ and Pb $4f_{7/2}$ indicates the interaction between CVE-Br and under-coordinated Pb^{2+} ions [49,55–57]. Similarly, the binding energies of Pb $4f_{5/2}$ and Pb $4f_{7/2}$ shift to lower binding energies of 142.6 eV and 137.9 eV upon CVE-DPA passivation, compared to the pristine perovskite film. This trend indicates interactions between undercoordinated Pb^{2+} ions and lone pair electrons of oxygen atoms in CVE-DPA, leading to the reduction of perovskite defects. [24,28,58,59] To confirm the formation of the Lewis adduct at the interface involving the methoxy group, we further analyzed and studied the binding energy of oxygen in the CVE-DPA molecule. Fig. S9 displays the O 1s spectra after spin-coating CVE-DPA onto the perovskite film and pristine CVE-DPA. The binding energy of O 1s in CVE-DPA upshift from 532.2 to 533.0 eV after the CVE-DPA deposited onto perovskite compared to pristine CVE-DPA. The results indicated that the oxygen in the molecule could act as an electron donating group, reacting with Pb^{2+}. That can stabilize the uncoordinated Pb^{2+}in perovskite. Furthermore, the N *1 s* XPS spectrum, shown in Fig. 5(b), revealed characteristic peaks related to the presence of ammonium groups (from FAI and MABr) in the perovskite. In the pristine perovskite, a peak at 402.0 eV (corresponding to $–NH_3$ in MA^{2+}) was observed. It was shifted to 401.6 eV upon the addition of CVE-Br. Additionally, compared to the control peak at 400.4 eV (attributed to $–N{=}H^{2+}$ in FA^{+}), the N *1s* peak shifted to 400.0 eV after adding CVE-Br. This shift in the N *1s* binding energy can be attributed to the bonding between the Br-functionalized end groups of CVE-Br and the $–NH_3$ and $–N{=}H^{2+}$ centers in the perovskite, leading to the formation of low-dimensional structures [55,60]. However, no observable shift in the N *1 s* binding energy was observed for CVE-DPA, which suggests a wrapping behavior of CVE-DPA around the perovskite rather than direct interaction. The I *3d* peak, shown in Fig. 5(c), also exhibited a similar shift towards lower binding energies. In Fig. S10, a peak at 71.3 eV was assigned to the C-Br bond in the perovskite, while the peaks at 69.4 eV and 68.2 eV corresponded to Br $3d_{3/2}$ and Br $3d_{5/2}$, respectively. In comparison to the control, the Br peaks in the CVE-Br film exhibited a shift towards lower binding energies of 70.9 eV, 69.1 eV, and 67.8 eV, respectively. A new peak associated with the C-Br bond in CVE-Br appeared at 69.9 eV. The XPS analysis of Pb, N, I, and Br confirmed the interaction between the Br atoms in CVE-Br and the perovskite, ascertaining the formation of low dimensional perovskite [55,57,61]. Conversely, the decreased XPS intensities of Pb, N, and I in CVE-DPA indicate the presence of a protective layer on the perovskite surface.

Photoluminescence (PL) and time-resolved photoluminescence (TRPL) measurements were performed on the perovskite layers containing CVE-Br and CVE-DPA to elucidate the charge carrier dynamics. The samples were excited using a 532 nm laser and the emission was detected at 770 nm. To provide further insight: if a molecule only performs defect passivation ability, PL spectrum intensity can be rationally expected to enhance due to a reduction in non-radiative recombination. Whereas a molecule holds both ability to passivate defect and facilitate charge transportation, carriers can be guide and transferred from the perovskite active layer to the transport layer. That is, the carrier transfer from perovskite to transporting layer predominate the decay process. The effectively carrier transfer leads to a decrease in PL intensity and shorten the decay time in TR-PL spectra.

The PL spectrum in Fig. 6(a) demonstrates that perovskite film with CVE-Br exhibits a significantly enhanced PL intensity compared to the control sample, indicating a reduction in non-radiative recombination due to effective defect passivation. On the other hand, perovskite film with CVE-DPA shows a remarkable quenching effect compared to the control, attributed to the incorporation of the 4,4‘-dimethoxy-diphenylamine group, which enhancing spatial interactions and improving hole mobility. Furthermore, the shift of the PL emission peak is also related to the defect passivation. Generally, the spontaneous radiative recombination caused by the trap states transition performs a red-shifted emission peak compared with that from the band to band transition. That is, reducing defect density in a film can lead to a blue-shift of PL

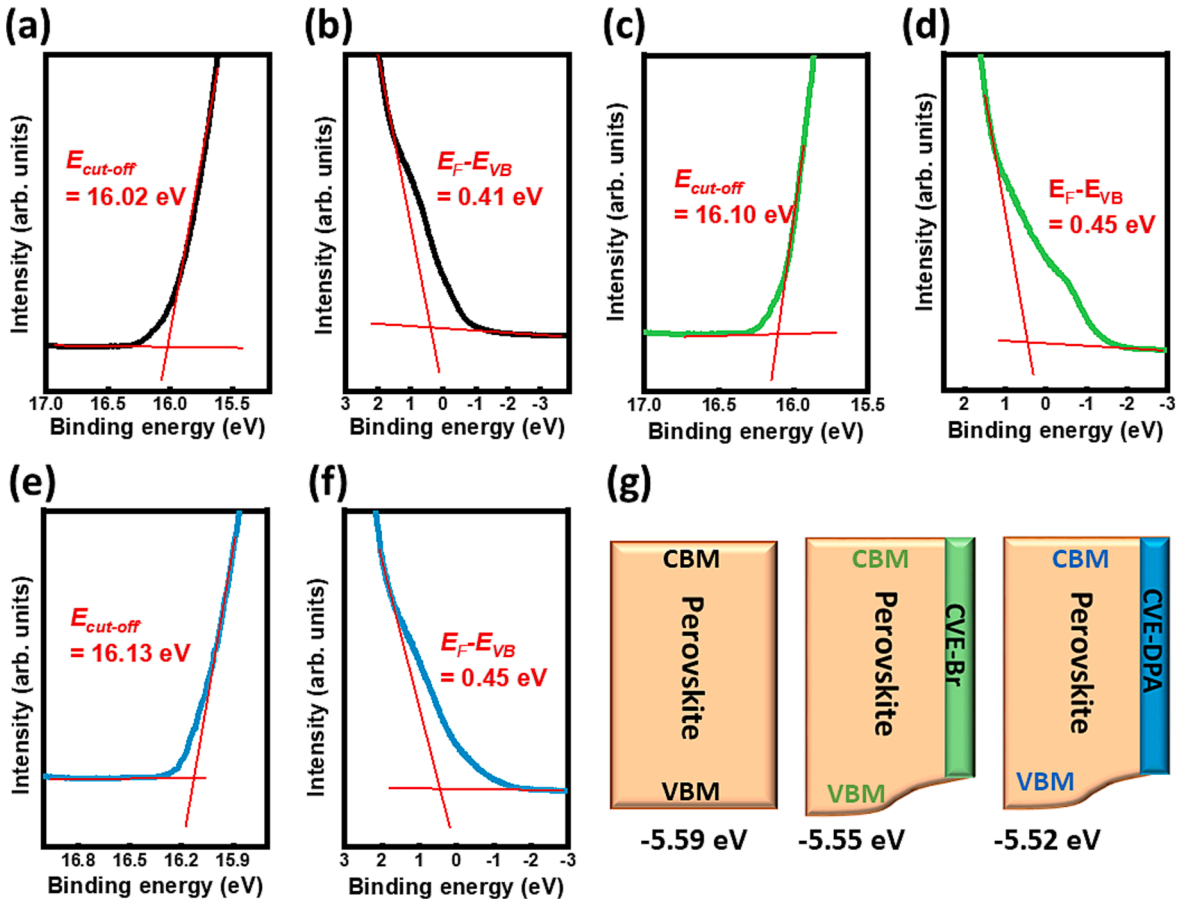

Fig. 4. UPS of perovskite layer (a, b) control (c, d) with CVE-Br and (e, f) with CVE-DPA. (g) Energy level diagram of control, CVE-Br and CVE-DPA perovskite films.

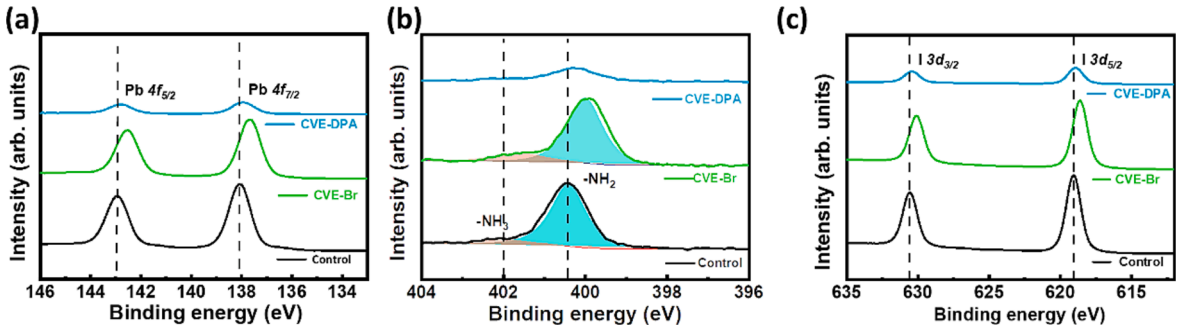

Fig. 5. High-resolution XPS peaks of control, CVE-Br, and CVE-DPA perovskite films of (a) Pb *4f*, (b) N *1 s*, and (c) I *3d*.

emission. [62] As seen in Fig. 6(a), both CVE-Br and CVE-DPA exhibit blue-shifted emission peaks, further confirming that CVE-Br and CVE-DPA can effectively passivate the defects on the perovskite surface. [29].

Finally, TRPL measurements are shown in Fig. 6(b, c), to identify the transient photoluminescence decay behavior of the carbazole derivatives. The decay curves are analyzed using a second-order decay kinetic model, and the fitting equation for the transient photoluminescence decay behavior is given by:

$$F(t) = A_1 exp\left(-\frac{t}{\tau_1}\right) + A_2 exp\left(-\frac{t}{\tau_2}\right) \quad (2)$$

$$\tau_{avg} = \frac{\sum_i A_i \tau_i}{\sum_i A_i} \quad (3)$$

where A_1 and A_2 represent the time-independent proportionality coefficients, τ_1 corresponds to the carrier transport time, and τ_2 represents the carrier recombination time.

By utilizing equation (3), the calculated average decay times for the carbazole derivatives are summarized in Table 1. The average decay time (τ_{avg}) of the perovskite film with CVE-Br increased for defect passivation because of a reduction in non-radiative recombination, leading to an increase in carrier lifetime. On the other hand, the addition of CVE-DPA (i.e., introducing 4,4'-dimethoxy-diphenylamine moiety) to the perovskite film facilitates efficient charge transfer, particularly for hole transport. Consequently, it results in a smaller τ_{avg} value, indicating effective and rapid carrier transfer, thereby reducing charge recombination. Also, a synergistic effect of carbazole derivatives and the hole transport material spiro-OMeTAD was achieved by spin-coating to form the hole transport layer. From Table 1, the decreasing τ_{avg} for the perovskite with CVE-Br/HTL means efficient and rapid carrier

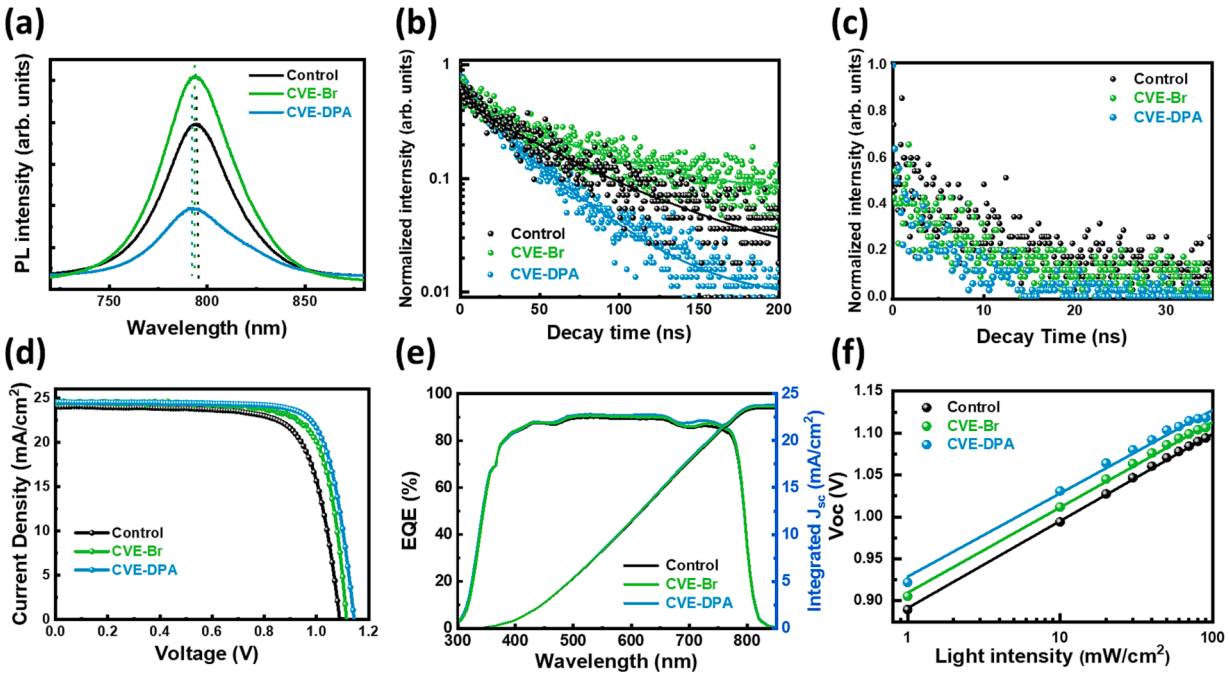

Fig. 6. (a) Steady-state PL spectra of control, CVE-Br, and CVE-DPA perovskite films on glass. (b) TRPL spectra of control, CVE-Br, and CVE-DPA perovskite films. (c) TRPL spectra of control, CVE-Br, and CVE-DPA perovskite films with HTL. (d) The *J-V* curves of the PSCs device with control, CVE-Br, and CVE-DPA. (e) EQE spectra and integrated current of control and carbazole derivatives PSCs devices. (f) Light intensity dependence of PSCs with control and carbazole derivatives.

Table 1
TRPL lifetime of control, CVE-Br and CVE-DPA perovskite films.

Sample	A_1 (%)	τ_1 (ns)	A_2 (%)	τ_2 (ns)	τ_{avg}	Hole diffusion length, L_D, (ns)
Control	37.6	6.19	62.4	57.55	38.23	738.33
CVE-Br	34.0	7.20	66.0	61.51	43.04	807.21
CVE-DPA	41.5	6.31	58.5	36.10	23.73	1047.38
Control + HTL	33.8	1.08	66.2	15.11	10.36	–
CVE-Br + HTL	34.5	1.10	65.5	15.01	10.21	–
CVE-DPA + HTL	56.0	0.88	44.0	7.44	3.70	–

extraction compared to the control, implying a reduction in non-radiative recombination. Furthermore, perovskite with CVE-DPA/HTL not only passivates the defects in the perovskite layer but also assists in the efficient transfer of holes from the active layer to spiro-OMeTAD through its side-chain 4,4'-dimethoxy-diphenylamine moiety. As a result, perovskite with CVE-DPA/HTL exhibits the fastest average decay time (τ_{avg}). Moreover, when the perovskite films are spin-coated with the hole transport layer, the carrier lifetimes of CVE-Br and CVE-DPA perovskite films (807.21 and 1047.38 ns, respectively) are longer compared to the control film (738.33 ns), as shown in Table 1. These results demonstrate that the addition of carbazole derivatives in the perovskite film can improve surface morphology and reduce defects, thereby enhancing charge transport. Additionally, the carrier diffusion length (L_D) can be calculated using the one-dimensional diffusion equation (4) [63]:

$$L_D \approx \frac{2d}{\pi}\sqrt{2\left(\frac{\tau}{\tau_{quench}} - 1\right)} \quad (4)$$

where the parameter d represents the thickness of the perovskite film, τ denotes the carrier lifetime in the absence of a transport layer, and τ_{quench} represents the carrier lifetime with the incorporation of a hole transport layer.

Subsequently, formal architecture perovskite solar cells (n-i-p) were fabricated to evaluate the impact of incorporating CVE-Br and CVE-DPA on the optoelectronic performance of PSCs (detailed device fabrication procedures are described in Supplementary Information). The schematic illustration of PSCs device is shown in Fig. S11. The *J-V* curves of the devices with various carbazole derivatives are presented in Fig. 6(d) and Fig. S12. The optimal concentration of CVE-DPA in the device is determined to be 10 mM, as shown in Fig. S13 and Table S3. The photovoltaic parameters are summarized in Table 2. Notably, the devices with CVE-DPA exhibited outstanding *PCE* of 22.05 %, with a short-circuit current density (J_{SC}) of 24.52 mA cm^{-2}, an open-circuit voltage (V_{OC}) of 1.14 V, and a fill factor (*FF*) of 78.62 %. These values are significantly higher than those of the control device (20.08 %) and the device with CVE-Br (21.01 %). Fig. 4(g) shows that the carbazole derivatives possess suitable energy levels. The XPS analysis, shown in Fig. 5, further supports the effective passivation of defects in the perovskite material by CVE-Br and CVE-DPA. The PL and TRPL measurements depicted in Fig. 6 (a-c) demonstrate that the incorporation of carbazole derivatives leads to a reduction in non-radiative recombination, facilitating efficient transport of holes from the perovskite layer to the hole transport layer. These findings collectively contribute to the notable enhancements observed in J_{SC}, V_{OC}, and *PCE* after adding carbazole derivatives.

Table 2
Average and optimal control and target device PV parameters under 1 sun irradiance (AM 1.5 G, 100 mW cm^{-2}).

Sample	V_{OC} (V)	J_{SC} (mA/cm^2)	*FF* (%)	*PCE* (%)
Control	1.08 ± 0.01 (1.10)	24.02 ± 0.51 (24.01)	76.11 ± 0.83 (76.49)	19.88 ± 0.52 (20.08)
CVE-Br	1.09 ± 0.01 (1.11)	24.20 ± 0.25 (24.54)	76.97 ± 0.95 (76.75)	20.45 ± 0.49 (21.01)
CVE-DPA	1.12 ± 0.01 (1.14)	24.60 ± 0.20 (24.52)	77.61 ± 0.56 (78.62)	21.40 ± 0.30 (22.05)

Moreover, the introduction of 4,4′-dimethoxy-diphenylamine groups onto CVE-DPA, as depicted in Fig. 6(c), further improves the hole transport properties within the device. This improvement can be attributed to the higher hole mobility, smoother film morphology, and reduced defect density in the CVE-DPA-based device, resulting in superior photovoltaic performance. Additionally, Fig. 6(e) presents the external quantum efficiency (EQE) spectra, which confirms that the J_{SC} values, with less than 5 % deviation, obtained from the *J-V* curves (control: 23.46 mA cm^{-2}, CVE-Br: 23.65 mA cm^{-2}, CVE-DPA: 23.82 mA cm^{-2}) align well with the EQE spectra. This agreement validates the absence of current stealing behavior. Overall, these results highlight the beneficial effects of incorporating carbazole derivatives on the photovoltaic performance of the perovskite solar cells, including reduced non-radiative recombination, improved hole transport, and enhanced overall device efficiency.

The dependence of the *J-V* characteristics on light intensity provides insights into the charge recombination mechanism in the PSCs with carbazole derivatives. Fig. 6(f) demonstrates a linear relationship between V_{OC} and light intensity. The relationship between V_{OC} and light intensity can be described by the following equation:

$$V_{oc} = V_s + \frac{nk_BT}{q} ln \frac{P}{P_s} \quad (5)$$

where V_{OC} is the open-circuit voltage at the standard light intensity (P_S = 100 mW/cm^2), n is the ideality factor, k_B is the Boltzmann constant, T is the absolute temperature (298.15 K), q is the elementary charge, P is a specific light intensity, and P_S is the standard light intensity. Fig. 6(f) illustrates the semi-logarithmic plot of V_{OC} versus light intensity, and the ideality factor (n) was determined by fitting V_{OC} values at various light intensities. The ideality factors for the device of control, CVE-Br, and CVE-DPA were 1.76, 1.70, and 1.65, respectively. A lower ideality factor indicates reduced dependence of V_{OC} on light intensity, suggesting suppressed charge recombination caused by interface defects. This observation highlights the excellent defect passivation achieved through the addition of CVE-DPA. The incorporation of CVE-DPA effectively mitigates defects in the perovskite material [64,65], leading to improved device performance.

Kelvin probe force microscopy (KPFM) was used to investigate the contact potential difference (CPD) and surface potential evolution under light illumination, shown in Fig. 7. CPD variations in the absorber layer are attributed to the excitation of electrons by photons with energies greater than E_g, causing them to transition from the valence band to the conduction band. The CPD is highly correlated with the light response and electron generation in the material. Therefore, larger CPD variations indicate better photovoltaic performance of the device, as it signifies the excitation of more charges. The addition of CVE-Br in perovskite film in the device leads to improved charge transport due to reduced defect generation. On the other hand, the incorporation of perovskite film with CVE-DPA not only passivates defects but also enhances charge mobility, resulting in the best charge transport capability.

For obtaining efficient photovoltaic devices, the chemical composition and the surface morphology are the essential criteria for fabricating an active layer from the macroscopic point of view. In comparison, the defects and carrier mobility in a photovoltaic device are key criteria of carrier transportation from the microscopic point of view. The space

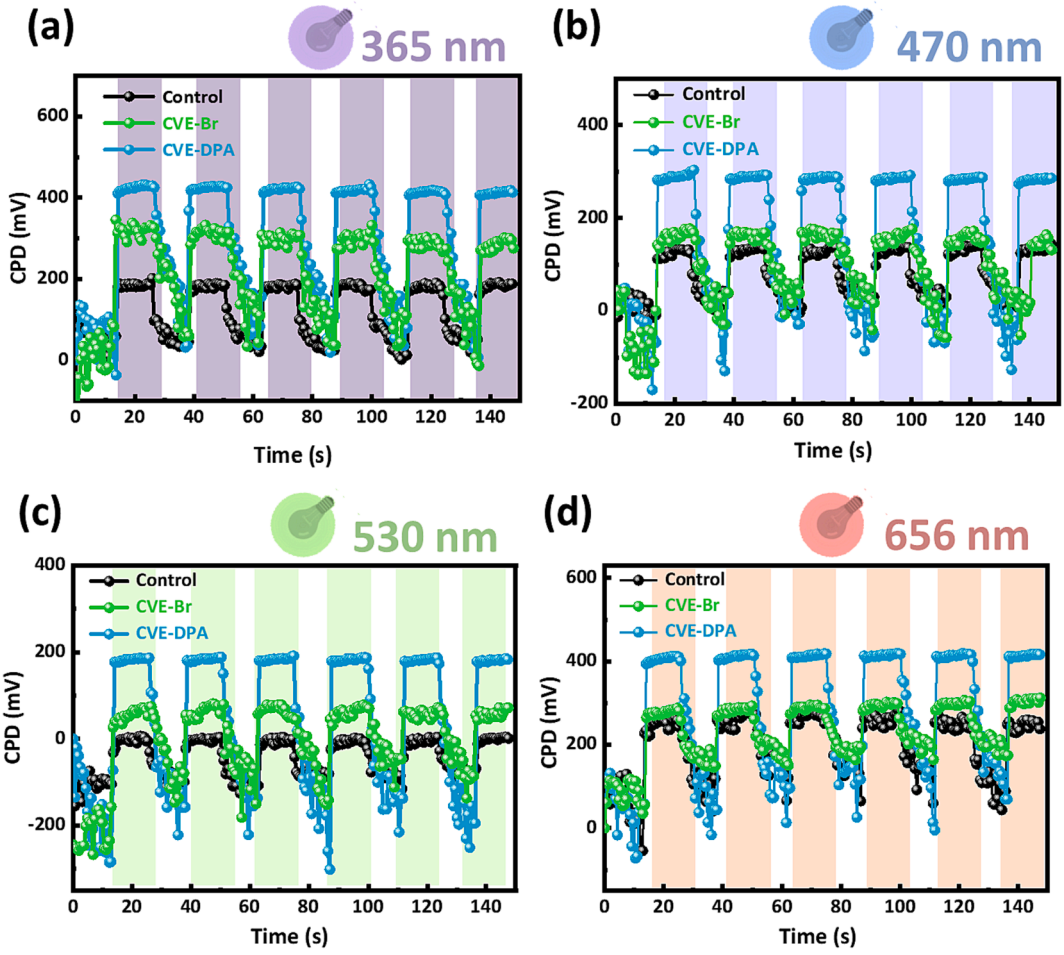

Fig. 7. The light-induced constant potential differences of control, CVE-Br, and CVE-DPA perovskite films were studied at various wavelengths of (a) 365 nm, (b) 470 nm, (c) 530 nm and (d) 656 nm.

charge limited current (SCLC) model is widely employed to elucidate the conductivity, trap density, and mobility of semiconductor thin films. *I-V* curves of devices with either pure electron or pure hole transport exhibit distinct regions: the ohmic region ($I \propto V$), the trap-filled limit (TFL) region ($I \propto V^n$, n > 2), and the Child's region ($I \propto V^2$). These regions provide valuable insights into the characteristics of devices. The ohmic region represents the linear relationship observed at low-bias voltages, indicating the presence of ohmic contacts. As the bias voltage increases, the current rises rapidly in a nonlinear manner, signifying the filling of trap states. The transition point corresponds to the trap-filled limit voltage (V_{TFL}), which indicates the voltage at which trap-filling occurs. The relationship between the trap-filled limit voltage and the trap density (N_t) can be described by the following equation:

$$V_{TFL} = \frac{eN_t d^2}{2\varepsilon\varepsilon_0} \tag{6}$$

where V_{TFL} represents the voltage at which trap states in the device are fully filled, while N_t denotes the trap density, e refers to the elementary charge, ε represents the dielectric constant of the perovskite material, ε_0 is the vacuum permittivity, and d corresponds to the thickness of the perovskite layer.

It is important to note that the trap density in the perovskite layer is considered to be the recombination or annihilation site for charge carriers. Once the carriers are captured, they undergo non-radiative recombination instead of being transferred to the respective charge transport layers, leading to a reduced photocurrent in the device. From Fig. 8(a), the V_{TFL} and trap density (N_t) values were calculated for the control, CVE-Br and CVE-DPA device to be 1.70×10^{16} cm^{-3}, 1.56×10^{16} and 1.43×10^{16} cm^{-3}, respectively, shown in Table S4. It can be inferred that CVE-Br and CVE-DPA effectively reduces the trap density. Additionally, the *I-V* curves in the ohmic region exhibit linear behavior at low bias voltages, as shown in Fig. 8(b). The conductivity can be calculated from the ohmic region using the following equation:

$$I = \sigma_0(\frac{A}{d})V \tag{7}$$

where A represents the active area, d is the film thickness, and σ_0 is the conductivity of the film.

The value of σ_0 for the CVE-Br and CVE-DPA device increased from 1.37×10^{-4} mS/cm to 2.82×10^{-4} mS/cm and 3.25×10^{-4} mS/cm. When the bias voltage continues to increase, the charge carrier mobility (μ) can be obtained in the Child's region of the *I-V* curve shown in Fig. 8(c) using Mott-Gurney's law:

$$J = \frac{9}{8}\mu\varepsilon\varepsilon_0(\frac{V^2}{d^3}) \tag{8}$$

where μ represents the charge carrier mobility, ε is the dielectric constant of perovskite, ε_0 is the dielectric constant of free space, and d is the thickness of perovskite.

After adding CVE-Br and CVE-DPA, the hole mobility increased from 2.28×10^{-3} cm^2/Vs to 2.41×10^{-3} cm^2/Vs and 2.64×10^{-3} cm^2/Vs, shown in Table S4. These results demonstrate that CVE-Br and CVE-DPA effectively enhance charge carrier extraction, reduce charge accumulation, and suppress recombination at the interface.

As mentioned, the hydrophobicity of the device is an important factor in determining the long-term stability of PSCs. The water contact angles of the CVE-Br-modified perovskite layer and the CVE-DPA-modified perovskite layer are measured 76.6° and 78.1°, respectively, which is superior to the contact angle of the pristine perovskite of 57.4°, shown in Fig. 9(a-c). The enlarged contact angle of the CVE-Br and CVE-DPA-modified perovskite layer confirms that introducing the CVE functional group onto the carbazole core can enhance their hydrophobicity.

To assess the device stability, the control PSCs and PSCs with CVE-DPA were stored at a relative humidity of 30 % and 25 °C. As shown in Fig. 9(d), the device with CVE-Br and CVE-DPA exhibited slower initial degradation compared to the control. After over 1,000 h of exposure, the PSCs with CVE-Br retained 84 % of their initial *PCE* and CVE-DPA retained 87 % of their initial *PCE*, while the control devices only retained 78 % of their initial *PCE*. These results indicate that carbazole derivatives can effectively protect the perovskite material from moisture-induced degradation, thereby improving the long-term stability of PSCs.

Finally, we summarized the photovoltaic performance of various carbazole derivatives-based PSCs in the past three years, as shown in Table S5. The photovoltaic performance of PSC can be effectively improved by using different functional groups. In contrast, CVE-DPA has demonstrated *PCE* levels that surpass the average and can be considered outstanding. This provides empirical evidence that the concurrent passivation of defects in the perovskite, coupled with the enhancement of hole transport capabilities, constitutes an effective approach.

3. Conclusion

We have synthesized and engineered carbazole-based molecules to enhance the performance of PSCs. These molecules include grafted bromine atoms and hydrophobic functional groups (CVE-Br) and grafted 4,4'-dimethoxy-diphenylamine groups (CVE-DPA). CVE-Br showcased compatible energy levels and effectively mitigated perovskite defects, consequently leading to an impressive increase in the PCE. In contrast, CVE-DPA possessed the dual advantage of suitable energy levels and high hole transport proficiency, as supported by photoluminescence (PL), transient photoluminescence (TRPL), and space charge limited current (SCLC) measurements. Moreover, CVE-DPA helped decrease defects and refined the perovskite film's texture by grafting methoxy groups onto it. This action passivated the perovskite surface defects, contributing synergistically to an impressive PCE of 22.05 %. Furthermore, the hydrophobicity of CVE-DPA ensures the improved long-term stability of PSCs. After 1000 h, the CVE-DPA device maintains 87 % of the initial efficiency.

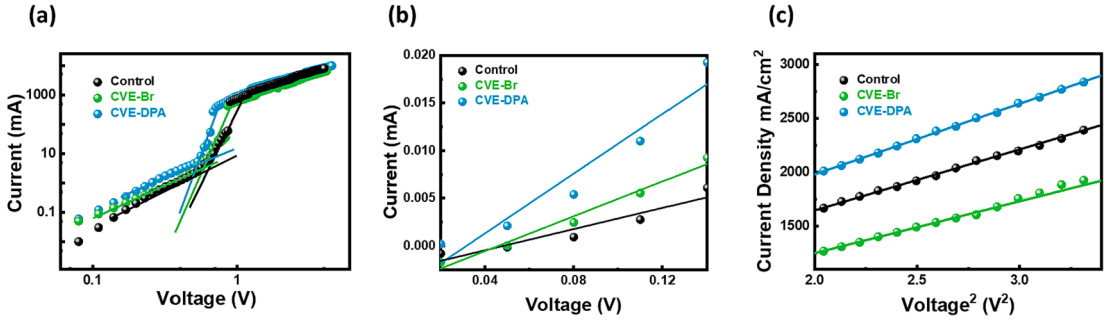

Fig. 8. The electronic property characterization of control PSCs, PSCs with CVE-Br and CVE-DPA. (a) The TFL voltage derived from SCLC measurement, (b) conductivity, and (c) mobility derived from the ohmic region and Child's region, respectively.

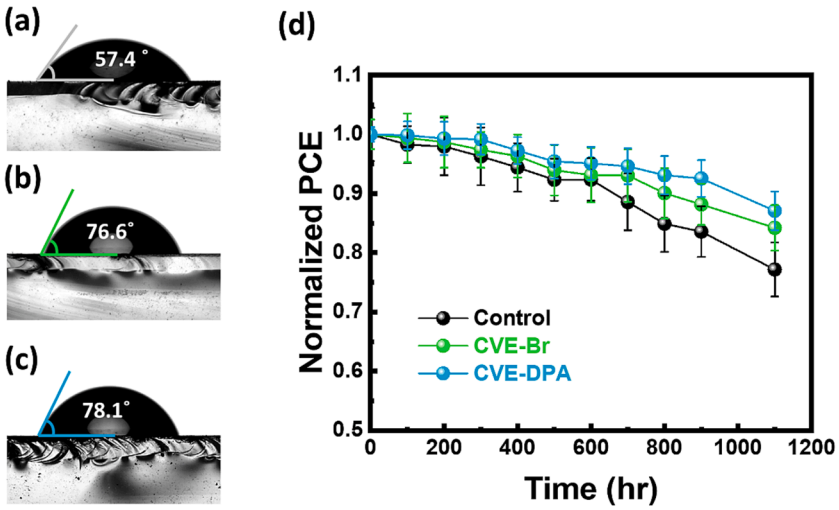

Fig. 9. Water contact angle of (a) control (i.e., perovskite), (b) CVE-Br perovskite film and (c) CVE-DPA perovskite film. (d) Stability test of PSCs devices with control, CVE-Br and CVE-DPA-modified perovskite layer under the ambient condition without encapsulation.

Declaration of Competing Interest

The authors declare that they have no known competing financial interests or personal relationships that could have appeared to influence the work reported in this paper.

Data availability

Data will be made available on request.

Acknowledgements

The authors thank Mei-Yueh Chien, Li-Mei Hsu and Chun-Tan Chang for providing valuable assistance on JEOL ECZ400S/L1, Agilent Technologies DD2 600 MHz NMR spectrometers, and MASS at the Instrument Center of National Chung Hsing University. The facility is operated under the grant of NSTC112-2740-M005-001. The authors also thank Dr. Ming-Tao Lee (BL-13A1), Dr. Jeng-Lun Chen (BL-17C1), Dr. Wei-Tsung Chuang (TLS-23A1), Dr. Chun-Jen Su (TLS-23A1) and Dr. Ting-Shan Chan (BL-01C1) at National Synchrotron Radiation Research Centre for useful discussion and suggestions, and Mr. Yung-Sheng Chen at Instrumentation Centre of National Tsing Hua University for TEM analysis. The authors appreciate the Microscopy Center at Chang Gung University for technical assistance. The author thanks the support from Center for Sustainability and Energy Technologies (CSET), Chang Gung University. The financial support from National Science and Technology Council, Taiwan (Project No. 111-2628-E-182-001-MY2, 111-2221-E-182-040-MY3, 111-2223-E-182-001-MY4, 110-2221-E-035-026, and 112-2221-E-035-004), Chang Gung University (URRPD2N0011) and Chang Gung Memorial Hospital at Linkou (CMRPD2N0061 and BMRPC74) are highly appreciated.

Appendix A. Supplementary data

Supplementary data to this article can be found online at https://doi.org/10.1016/j.cej.2023.147208.

References

[1] Y. Wu, H. Zhu, B.-B. Yu, S. Akin, Y. Liu, Z. Shen, L. Pan, H. Cai, Interface modification to achieve high-efficiency and stable perovskite solar cells, Chem. Eng. J. 433 (2022), https://doi.org/10.1016/j.cej.2022.134613.

[2] H. Su, L. Zhang, Y. Liu, Y. Hu, B. Zhang, J. You, X. Du, J. Zhang, X. Ren, J. Gou, S. Liu, Polarity regulation for stable 2D-perovskite-encapsulated high-efficiency 3D-perovskite solar cells, Nano Energy 95 (2022), https://doi.org/10.1016/j.nanoen.2022.106965.

[3] W. Zhao, M. Wu, Z. Liu, S. Yang, Y. Li, J. Wang, L. Yang, Y. Han, S. Liu, Orientation engineering via 2D seeding for stable 24.83 % efficiency perovskite solar cells, Adv. Energy Mater. 13 (14) (2023), https://doi.org/10.1002/aenm.202204260.

[4] National Renewable Energy Laboratory, "Best research-cell efficiency chart https://www.nrel.gov/pv/cell-efficiency.html, 2023 (accessed 26 September 2023).

[5] H. Min, D.Y. Lee, J. Kim, G. Kim, K.S. Lee, J. Kim, M.J. Paik, Y.K. Kim, K.S. Kim, M. G. Kim, T.J. Shin, S. Il Seok, Perovskite solar cells with atomically coherent interlayers on SnO_2 electrodes, Nature 598(7881) (2021) 444-450. https://doi.org/10.1038/s41586-021-03964-8.

[6] J. Jeong, M. Kim, J. Seo, H. Lu, P. Ahlawat, A. Mishra, Y. Yang, M.A. Hope, F. T. Eickemeyer, M. Kim, Y.J. Yoon, I.W. Choi, B.P. Darwich, S.J. Choi, Y. Jo, J. H. Lee, B. Walker, S.M. Zakeeruddin, L. Emsley, U. Rothlisberger, A. Hagfeldt, D. S. Kim, M. Gratzel, J.Y. Kim, Pseudo-halide anion engineering for alpha-$FAPbI_3$ perovskite solar cells, Nature 592 (7854) (2021) 381–385, https://doi.org/10.1038/s41586-021-03406-5.

[7] C. Ran, J. Xu, W. Gao, C. Huang, S. Dou, Defects in metal triiodide perovskite materials towards high-performance solar cells: origin, impact, characterization, and engineering, Chem. Soc. Rev. 47 (12) (2018) 4581–4610, https://doi.org/10.1039/c7cs00868f.

[8] A. Hassan, Z. Wang, Y.H. Ahn, M. Azam, A.A. Khan, U. Farooq, M. Zubair, Y. Cao, Recent defect passivation drifts and role of additive engineering in perovskite photovoltaics, Nano Energy 101 (2022), https://doi.org/10.1016/j.nanoen.2022.107579.

[9] B. Chen, P.N. Rudd, S. Yang, Y. Yuan, J. Huang, Imperfections and their passivation in halide perovskite solar cells, Chem. Soc. Rev. 48 (14) (2019) 3842–3867, https://doi.org/10.1039/c8cs00853a.

[10] Z. Yang, X. Cao, G. Niu, Y. Wang, Y. Dong, S. Cao, W. Liu, X. Wang, Y. Liu, J. Wang, Removing residual PbI_2 on the perovskite surface for efficient solar cells, Chem. Eng. J. 464 (2023), https://doi.org/10.1016/j.cej.2023.142720.

[11] Y. Chen, Q. Meng, Y. Xiao, X. Zhang, J. Sun, C.B. Han, H. Gao, Y. Zhang, Y. Lu, H. Yan, Mechanism of PbI_2 in situ passivated perovskite films for enhancing the performance of perovskite solar cells, ACS Appl. Mater. Interfaces 11 (47) (2019) 44101–44108, https://doi.org/10.1021/acsami.9b13648.

[12] T.J. Jacobsson, J.P. Correa-Baena, E. Halvani Anaraki, B. Philippe, S.D. Stranks, M. E. Bouduban, W. Tress, K. Schenk, J. Teuscher, J.E. Moser, H. Rensmo, A. Hagfeldt, Unreacted PbI_2 as a double-edged sword for enhancing the performance of perovskite solar cells, J. Am. Chem. Soc. 138(32) (2016) 10331-43. https://doi.org/10.1021/jacs.6b06320.

[13] W.H. Zhang, L. Chen, Z.P. Zou, Z.A. Nan, J.L. Shi, Q.P. Luo, Y. Hui, K.X. Li, Y. J. Wang, J.Z. Zhou, J.W. Yan, B.W. Mao, Defect passivation by a multifunctional phosphate additive toward improvements of efficiency and stability of perovskite solar cells, ACS Appl. Mater. Interfaces 14 (28) (2022) 31911–31919, https://doi.org/10.1021/acsami.2c05956.

[14] J. Zhou, M. Li, S. Wang, L. Tan, Y. Liu, C. Jiang, X. Zhao, L. Ding, C. Yi, 2-CF_3-PEAI to eliminate Pb^0 traps and form a 2D perovskite layer to enhance the performance and stability of perovskite solar cells, Nano Energy 95 (2022), https://doi.org/10.1016/j.nanoen.2022.107036.

[15] L. Wang, H. Zhou, J. Hu, B. Huang, M. Sun, B. Dong, G. Zheng, Y. Huang, Y. Chen, L. Li, Z. Xu, N. Li, Z. Liu, Q. Chen, L.-D. Sun, C.-H. Yan, A Eu3+-Eu2+ ion redox shuttle imparts operational durability to Pb-I perovskite solar cells, Science 363 (6424) (2019) 265–270, https://doi.org/10.1126/science.aau5701.

[16] J. Xia, C. Liang, H. Gu, S. Mei, S. Li, N. Zhang, S. Chen, Y. Cai, G., Xing, Surface passivation toward efficient and stable perovskite solar cells, Energy & Environmental Materials 6 (1) (2022), https://doi.org/10.1002/eem2.12296.

[17] N.K. Noel, A. Abate, S.D. Stranks, E.S. Parrott, V.M. Burlakov, A. Goriely, H. J. Snaith, Enhanced photoluminescence and solar cell performance via lewis base passivation of organic–inorganic lead halide perovskites, ACS Nano 8 (10) (2014) 9815–9821, https://doi.org/10.1021/nn5036476.
[18] M. Xia, Y. Xia, Z. Zheng, X. Chen, J. Yang, J. Du, A. Mei, Y. Hu, H. Han, Defect passivation by a sulfur-containing lewis base for efficient printable mesoscopic perovskite solar cells, Solar RRL 6 (12) (2022), https://doi.org/10.1002/solr.202200802.
[19] G. Qu, D. Khan, F. Yan, A. Atsay, H. Xiao, Q. Chen, H. Xu, I. Nar, Z.-X. Xu, Reformation of thiophene-functionalized phthalocyanine isomers for defect passivation to achieve stable and efficient perovskite solar cells, J. Energy Chem. 67 (2022) 263–275, https://doi.org/10.1016/j.jechem.2021.09.041.
[20] G. Tumen-Ulzii, M. Auffray, D. Klotz, G.F. Harrington, X.-K. Chen, U. Balijapalli, V. Vediyappan, N. Nakamura, Z. Feng, K. Takekuma, Y. Fujita, P. Wang, S. Yamada, K. Tamada, M. Batmunkh, Y.L. Zhong, F. Mathevet, H. Salway, M. Anaya, S.D. Stranks, T. Matsushima, C. Adachi, Defect passivation by pyridine-carbazole molecules for efficient and stable perovskite solar cells, ACS Appl. Energy Mater. 5 (12) (2022) 15819–15827, https://doi.org/10.1021/acsaem.2c03364.
[21] X. Ding, H. Wang, C. Chen, H. Li, Y. Tian, Q. Li, C. Wu, L. Ding, X. Yang, M. Cheng, Passivation functionalized phenothiazine-based hole transport material for highly efficient perovskite solar cell with efficiency exceeding 22 %, Chem. Eng. J. 410 (2021) https://doi.org/10.1016/j.cej.2020.128328.
[22] S.S. Reddy, V.M. Arivunithi, V.G. Sree, H. Kwon, J. Park, Y.-C. Kang, H. Zhu, Y.-Y. Noh, S.-H. Jin, Lewis acid-base adduct-type organic hole transport material for high performance and air-stable perovskite solar cells, Nano Energy 58 (2019) 284–292, https://doi.org/10.1016/j.nanoen.2019.01.041.
[23] Z. Zhang, W. Fu, H. Ding, H.-X. Ju, K. Yan, X. Zhang, F. Ding, C.-Z. Li, H. Chen, Modulate molecular interaction between hole extraction polymers and lead ions toward hysteresis-free and efficient perovskite solar cells, Adv. Mater. Interfaces 5 (15) (2018), https://doi.org/10.1002/admi.201800090.
[24] S.J. Park, S. Jeon, I.K. Lee, J. Zhang, H. Jeong, J.-Y. Park, J. Bang, T.K. Ahn, H.-W. Shin, B.-G. Kim, H.J. Park, Inverted planar perovskite solar cells with dopant free hole transporting material: Lewis base-assisted passivation and reduced charge recombination, J. Mater. Chem. A 5 (25) (2017) 13220–13227, https://doi.org/10.1039/c7ta02440a.
[25] Z. Cui, Y. Wang, Y. Chen, X. Chen, X. Deng, W. Chen, C. Shi, Soluble tetra-methoxyltriphenylamine substituted zinc phthalocyanine as dopant-free hole transporting materials for perovskite solar cells, Org. Electron. 69 (2019) 248–254, https://doi.org/10.1016/j.orgel.2019.03.035.
[26] C. Hanmandlu, R. Paste, H. Tsai, S.N.S. Yadav, K.-W. Lai, Y.-Y. Wang, C. S. Gantepogu, C.-H. Hou, J.-J. Shyue, Y.-J. Lu, T.S. Jadhav, J.-M. Liao, H.-H. Chou, H.Q. Wong, T.-J. Yen, C.-S. Lai, D. Ghosh, S. Tretiak, H.-J. Yen, C.-W. Chu, 3D nanographene precursor suppress interfacial recombination in PEDOT: PSS based perovskite solar cells, Nano Energy 107 (2023), https://doi.org/10.1016/j.nanoen.2022.108136.
[27] N. Minoi, F. Ishiwari, K. Murotani, R. Nishikubo, T. Fukushima, A. Saeki, Surface Passivation of lead halide perovskite solar cells by a bifacial donor−π–donor molecule, ACS Appl. Mater. Interfaces 15 (5) (2023) 6708–6715, https://doi.org/10.1021/acsami.2c18446.
[28] X. Zhou, J. Qiu, J. Li, W. Qi, Y. Li, S. Jiao, H. Ling, P. Wang, F. Liu, K. Sohail, J. Li, G. Wang, X. Chen, G. Hou, J. Luo, X. Zhang, Y. Zhao, Y. Li, X. Zhang, Reduced defects and enhanced Vbi in perovskite absorbers through synergetic passivating effect using 4-methoxyphenylacetic acid, J. Power Sources 518 (2022), https://doi.org/10.1016/j.jpowsour.2021.230734.
[29] X. Ji, T. Zhou, Q. Fu, W. Wang, Z. Wu, M. Zhang, X. Guo, D. Liu, H.Y. Woo, Y. Liu, Dopant-free two-dimensional hole transport small molecules enable efficient perovskite solar cells, Adv. Energy Mater. 13 (11) (2023), https://doi.org/10.1002/aenm.202203756.
[30] Z. Li, B. Li, X. Wu, S.A. Sheppard, S. Zhang, D. Gao, N.J. Long, Z. Zhu, Organometallic-functionalized interfaces for highly efficient inverted perovskite solar cells, Science 376 (6591) (2022) 416–420, https://doi.org/10.1126/science.abm8566.
[31] C. Lu, M. Aftabuzzaman, C. Hoon Kim, H. Kyu Kim, Novel trifluoropropoxy-substituted asymmetric carbazole derivatives as efficient and hydrophobic hole transporting materials for high-performance and stable perovskite solar cells, Chem. Eng. J. 428 (2022), https://doi.org/10.1016/j.cej.2021.131108.
[32] N.J. Jeon, J.H. Noh, W.S. Yang, Y.C. Kim, S. Ryu, J. Seo, S.I. Seok, Compositional engineering of perovskite materials for high-performance solar cells, Nature 517 (7535) (2015) 476–480, https://doi.org/10.1038/nature14133.
[33] R. Zheng, S. Zhao, H. Zhang, H. Li, J. Zhuang, X. Liu, H. Li, H. Wang, Defect passivation grain boundaries using 3-aminopropyltrimethoxysilane for highly efficient and stable perovskite solar cells, Sol. Energy 224 (2021) 472–479, https://doi.org/10.1016/j.solener.2021.06.001.
[34] Q. Jiang, Y. Zhao, X. Zhang, X. Yang, Y. Chen, Z. Chu, Q. Ye, X. Li, Z. Yin, J. You, Surface passivation of perovskite film for efficient solar cells, Nat. Photonics 13 (7) (2019) 460–466, https://doi.org/10.1038/s41566-019-0398-2.
[35] M. Li, J. Zhou, L. Tan, Y. Liu, S. Wang, C. Jiang, H. Li, X. Zhao, X. Gao, W. Tress, L. Ding, C. Yi, Brominated PEAI as multi-functional passivator for high-efficiency perovskite solar cell, Energy Environ. Mater. (2022), https://doi.org/10.1002/eem2.12360.
[36] T.M. Koh, V. Shanmugam, X. Guo, S.S. Lim, O. Filonik, E.M. Herzig, P. Müller-Buschbaum, V. Swamy, S.T. Chien, S.G. Mhaisalkar, N. Mathews, Enhancing moisture tolerance in efficient hybrid 3D/2D perovskite photovoltaics, J. Mater. Chem. A 6 (5) (2018) 2122–2128, https://doi.org/10.1039/c7ta09657g.
[37] S. You, F.T. Eickemeyer, J. Gao, J.-H. Yum, X. Zheng, D. Ren, M. Xia, R. Guo, Y. Rong, S.M. Zakeeruddin, K. Sivula, J. Tang, Z. Shen, X. Li, M. Grätzel, Bifunctional hole-shuttle molecule for improved interfacial energy level alignment and defect passivation in perovskite solar cells, Nat. Energy 8 (5) (2023) 515–525, https://doi.org/10.1038/s41560-023-01249-0.
[38] B. Zhao, X. Yan, T. Zhang, X. Ma, C. Liu, H. Liu, K. Yan, Y. Chen, X. Li, Introduction of multifunctional triphenylamino derivatives at the perovskite/HTL interface to promote efficiency and stability of perovskite solar cells, ACS Appl. Mater. Interfaces 12 (8) (2020) 9300–9306, https://doi.org/10.1021/acsami.9b21112.
[39] Q. Fu, X. Tang, Y. Gao, H. Liu, M. Chen, R. Wang, Z. Song, Y. Yang, J. Wang, Y. Liu, Dimensional tuning of perylene diimide-based polymers for perovskite solar cells with over 24 % efficiency, Small 19 (24) (2023) e2301175.
[40] A. Jegorovė, M.A. Truong, R. Murdey, M. Daskeviciene, T. Malinauskas, K. Kantminiene, V. Jankauskas, V. Getautis, A. Wakamiya, Starburst carbazole derivatives as efficient hole transporting materials for perovskite solar cells, Solar RRL 6 (1) (2021), https://doi.org/10.1002/solr.202100877.
[41] G. You, L. Li, S. Wang, J. Cao, L. Yao, W. Cai, Z. Zhou, K. Li, Z. Lin, H. Zhen, Q. Ling, Donor–acceptor type polymer bearing carbazole side chain for efficient dopant-free perovskite solar cells, Adv. Energy Mater. 12 (2) (2021), https://doi.org/10.1002/aenm.202102697.
[42] X. Zhang, H. Tang, D. Hu, T. Li, H. Wang, X. Zhu, W. Ma, S. Li, T. Zhu, Ambient-air-stable inverted perovskite solar cells by carbazole analog tailored perovskite thin films, Solar RRL (2023), https://doi.org/10.1002/solr.202300051.
[43] X.-D. Zhu, F. Wu, C.-C. Peng, L.-Y. Ding, Y.-J. Yu, Z.-Q. Jiang, L.-N. Zhu, L.-S. Liao, Asymmetrical planar acridine-based hole-transporting materials for highly efficient perovskite solar cells, Chem. Eng. J. 413 (2021), https://doi.org/10.1016/j.cej.2020.127440.
[44] Y.-C. Chen, J.-H. Yen, C.-L. Chung, C.-P. Chen, Methoxy groups on bifluorenylidene-based hole transporting materials result in highly efficient and stable dopant-free inverted perovskite solar cells, Sol. Energy 179 (2019) 371–379, https://doi.org/10.1016/j.solener.2019.01.008.
[45] K. Chen, H. Lu, Y. Yang, S. Li, K. Jia, F. Wu, L. Zhu, Simultaneously modifying hole transport material and perovskite via a crown ether-based semiconductor toward efficient and stable perovskite solar cells, Solar RRL 7 (4) (2022), https://doi.org/10.1002/solr.202200987.
[46] L. Yangi, Y. Li, Y. Pei, J. Wang, H. Lin, X. Li, A novel 2D perovskite as surface "patches" for efficient flexible perovskite solar cells, J. Mater. Chem. A 8 (16) (2020) 7808–7818, https://doi.org/10.1039/c9ta13719j.
[47] S. Wang, F. Cao, Y. Wu, X. Zhang, J. Zou, Z. Lan, W. Sun, J. Wu, P. Gao, Multifunctional 2D perovskite capping layer using cyclohexylmethylammonium bromide for highly efficient and stable perovskite solar cells, Mater. Today Phys. 21 (2021), https://doi.org/10.1016/j.mtphys.2021.100543.
[48] N. Zhou, Y. Shen, L. Li, S. Tan, N. Liu, G. Zheng, Q. Chen, H. Zhou, Exploration of crystallization kinetics in quasi two-dimensional perovskite and high performance solar cells, J. Am. Chem. Soc. 140 (1) (2018) 459–465, https://doi.org/10.1021/jacs.7b11157.
[49] S. Zhan, Y. Duan, Z. Liu, L. Yang, K. He, Y. Che, W. Zhao, Y. Han, S. Yang, G. Zhao, N. Yuan, J. Ding, S. Liu, Stable 24.29 %-efficiency FA0.85MA0.15PbI3 perovskite solar cells enabled by methyl haloacetate-lead dimer complex, Adv. Energy Mater. 12 (27) (2022), https://doi.org/10.1002/aenm.202200867.
[50] N. Widjonarko, Introduction to advanced X-ray diffraction techniques for polymeric thin films, Coatings 6 (4) (2016), https://doi.org/10.3390/coatings6040054.
[51] Y. Choi, D. Koo, G. Jeong, U. Kim, H. Kim, F. Huang, H. Park, A vertically oriented two-dimensional Ruddlesden-Popper phase perovskite passivation layer for efficient and stable inverted perovskite solar cells, Energy Environ. Sci. 15 (8) (2022) 3369–3378, https://doi.org/10.1039/d2ee00759b.
[52] C. Liu, J. He, M. Wu, Y. Wu, P. Du, L. Fan, Q. Zhang, D. Wang, T. Zhang, All-inorganic CsPbI2Br perovskite solar cell with open-circuit voltage over 1.3 V by balancing electron and hole transport, Solar RRL 4 (7) (2020), https://doi.org/10.1002/solr.202000016.
[53] Y. Wang, X. Wang, C. Wang, R. Cheng, L. Zhao, X. Wang, X. Zhang, J. Shang, H. Zhang, L. Zhao, Y. Tu, W. Huang, Defect suppression and energy level alignment in formamidinium-based perovskite solar cells, J. Energy Chem. 67 (2022) 65–72, https://doi.org/10.1016/j.jechem.2021.09.043.
[54] L. Canil, T. Cramer, B. Fraboni, D. Ricciarelli, D. Meggiolaro, A. Singh, M. Liu, M. Rusu, C.M. Wolff, N. Phung, Q. Wang, D. Neher, T. Unold, P. Vivo, A. Gagliardi, F. De Angelis, A. Abate, Tuning halide perovskite energy levels, Energy Environ. Sci. 14 (3) (2021) 1429–1438, https://doi.org/10.1039/d0ee02216k.
[55] S.Y. Abate, S. Jha, G. Ma, J. Nash, N. Pradhan, X. Gu, D. Patton, Q. Dai, Surface capping layer prepared from the bulky tetradodecylammonium bromide as an efficient perovskite passivation layer for high-performance perovskite solar cells, ACS Appl. Mater. Interfaces 14 (51) (2022) 56900–56909, https://doi.org/10.1021/acsami.2c19201.
[56] X. Sun, L. Shi, Y. Zhang, H. Yuan, K. Zhang, L. Duan, Q. Li, Z. Huang, X. Ban, D. Zhang, Synergistic modification of benzimidazole and bromohexyl for highly efficient and stable perovskite solar cells, Chem. Eng. J. 453 (2023), https://doi.org/10.1016/j.cej.2022.139698.
[57] R. He, T. Chen, Z. Xuan, T. Guo, J. Luo, Y. Jiang, W. Wang, J. Zhang, X. Hao, L. Wu, Y. Wang, I. Constantinou, S. Ren, D. Zhao, Efficient wide-bandgap perovskite solar cells enabled by doping a bromine-rich molecule, Nanophotonics 10 (8) (2021) 2059–2068, https://doi.org/10.1515/nanoph-2020-0634.
[58] Z. Zhang, C. Wang, F. Li, L. Liang, L. Huang, L. Chen, Y. Ni, P. Gao, H. Wu, Bifunctional cellulose interlayer enabled efficient perovskite solar cells with simultaneously enhanced efficiency and stability, Adv. Sci. (Weinh) 10 (8) (2023) e2207202.

[59] Y. Tan, H. Cheng, Y. Zhao, L. Wan, Z.-S. Wang, Indolocarbazole-core linked triphenylamine as an interfacial passivation layer for perovskite solar cells, J. Mater. Chem. A 10 (13) (2022) 7173–7185, https://doi.org/10.1039/d2ta00499b.
[60] S. Ning, S. Zhang, J. Sun, C. Li, J. Zheng, Y.M. Khalifa, S. Zhou, J. Cao, Y. Wu, Ambient pressure X-ray photoelectron spectroscopy investigation of thermally stable halide perovskite solar cells via post-treatment, ACS Appl. Mater. Interfaces 12 (39) (2020) 43705–43713, https://doi.org/10.1021/acsami.0c12044.
[61] X. Sun, B. He, J. Zhu, R. Zhu, H. Chen, Y. Duan, Q. Tang, Multifunctional brominated graphene oxide boosted charge extraction for high-efficiency and stable all-inorganic CsPbBr 3 perovskite solar cells, Chem. Eng. J. 412 (2021), https://doi.org/10.1016/j.cej.2021.128727.
[62] Y. Shao, Z. Xiao, C. Bi, Y. Yuan, J. Huang, Origin and elimination of photocurrent hysteresis by fullerene passivation in $CH_3NH_3PbI_3$ planar heterojunction solar cells, Nat. Commun. 5 (2014) 5784, https://doi.org/10.1038/ncomms6784.
[63] A.H. Proppe, R. Quintero-Bermudez, H. Tan, O. Voznyy, S.O. Kelley, E.H. Sargent, Synthetic control over quantum well width distribution and carrier migration in low-dimensional perovskite photovoltaics, J. Am. Chem. Soc. 140 (8) (2018) 2890–2896, https://doi.org/10.1021/jacs.7b12551.
[64] V. Gupta, A.K. Kyaw, D.H. Wang, S. Chand, G.C. Bazan, A.J. Heeger, Barium: an efficient cathode layer for bulk-heterojunction solar cells, Sci. Rep. 3 (2013) 1965, https://doi.org/10.1038/srep01965.
[65] F. Xie, C.-C. Chen, Y. Wu, X. Li, M. Cai, X. Liu, X. Yang, L. Han, Vertical recrystallization for highly efficient and stable formamidinium-based inverted-structure perovskite solar cells, Energy Environ. Sci. 10 (9) (2017) 1942–1949, https://doi.org/10.1039/c7ee01675a.